Mathematics

Research article

Minimum length scale control in thermal-mechanical coupled topology optimization based on phase field method

Qian Yu[1], **Yuyan Liu**[2] **and Mingyuan Yang**[1,*]

[1] School of Mathematical Sciences, Peking University, Beijing 100871, China

[2] Department of Statistics, Rice University, 6100 Main St, Houston, TX 77005, USA

* **Correspondence:** Email: mingyuanyang@pku.edu.cn.

Abstract: This paper focuses on topology optimization for additive manufacturing, where the minimum length scale of designs must be greater than the nozzle's length scale. We present a general framework for controlling the minimum length scale in topology optimization using the phase field method, which is applicable to mechanical, heat transfer, and thermal-mechanical coupled topology optimization. The proposed method introduces an energy functional as the objective function of topology optimization, which includes the surface free energy, strain energy, volume constraints, minimum length scale constraints, and necessary boundary terms to satisfy the equilibrium condition of elasticity. A newly defined convolution operation $\mathcal{B}_r$ (where r is the radius related to the length scale) is combined with established skeleton extraction techniques to achieve control over the minimum length scale. At the same time, the skeletons of new designs are preserved in a way that is consistent with those obtained from designs without size control. To find the minimum of the constructed energy functional, the augmented Lagrangian method is first used to derive the extremum functional. Then the stationary point of the extremum functional is transformed into the solution of a time-dependent Allen-Cahn type equation, which effectively converts the topology optimization problem into solving partial differential equations. An operator-splitting-based hybrid numerical method is proposed to solve the Allen-Cahn type equation. The numerical results of mechanical, heat transfer, and thermal-mechanical coupled topology optimizations are presented to demonstrate the efficiency and scalability of the proposed minimum length scale control framework.

1. Introduction

Additive manufacturing, a relatively new and rapidly evolving production technology, faces critical technological constraints, such as the minimum printable size [1–3]. In order to ensure that the optimized design is immediately manufacturable, it is essential to take the length scale constraints into account during topology optimization [4, 5], which also helps to improve the regularity of topology optimization [6]. Sigmund [7] originally pointed out that perimeter control and mesh-independent filtering were the two most promising approaches to deal with the numerical instabilities in topology optimization. Mesh-independent filtering combined with projection [8], for its simple implementation, as an efficient heuristic rule, is commonly used to eliminate small, undesirable features to achieve minimum length scale control. For example, Li et al. [9] redefined some weight coefficients which were different from those used in the density filtering and projection, to calculate the average density of elements within a small circular region, and applied P-norm or P-mean functionals to penalize the minimum length scale constraints. A similar approach is applied on length scale control in density-based multi-material topology optimization [10]. Huang and Liu [11] used the Helmholtz-type partial differential equation (PDE) filter and the Heaviside projection, combining the heat method, a skeleton extraction technique, to achieve the desired maximum and minimum length scale control. While for perimeter control, despitel its theoretical proof in existence and convergence that mesh-independent filtering lacks [7], it can be a little difficult to establish its characteristic length scale, and the results can be improved by combining it with filtering techniques [12–14].

Perimeter control is often used in level set topology optimization because the level set can explicitly or implicitly track structural boundaries. However, perimeter control in the level set framework does not suffice to control the length scale of the optimized design, which is commonly used to prevent the emergence of irregular geometric features. Additionally, the level set framework requires extra techniques to create holes [15]. To deal with these problems, Barrera et al. [13] introduced two sets of independent optimization variables, level set variables and density variables, to enable nucleation. The minimum feature size of optimized designs can be controlled by the radius of the linear filter applied to the density variables. Jansen [12] also combined the level set method with the density-based method. He adopted geometric constraints similar to those that had been proposed in the framework of density-based topology optimization with projection filters [16] to formulate equivalent length scale optimization problems. Zhou et al. [17] used the level set to characterize hole features and imposed extra constraints on the holes' number, shape, size, and spacing, to achieve the desired size control. However, these types of level set topology optimization come at the cost of a more complex problem formulation and additional computational costs due to an increased number of optimization variables.

The Phase field method [18–20] has gained prominence in topology optimization in recent years due to its perimeter control. An important characteristic of the phase field method is its energy dissipation during phase transition [21, 22] or topological changes. The order parameter of the phase field method, ranging within [0, 1], can be directly viewed as density variables similar to density-based topology optimization [23,24], resulting in existence of a diffuse interface or a fictitious region in (0, 1). However, as the diffuse interfacial coefficient $\epsilon \to 0$, the problem of minimizing free energy can be approximated as a minimal perimeter problem, which helps ensure a well-posed design problem and allows control over the number of holes, thus establishing a characteristic length scale [25]. Compared to the level set method, the phase field method offers computational simplicity, as it does not require

the re-initialization and introduction of two sets of independent optimization variables to enable the nucleation. The Allen–Cahn model, one of the most well-known phase field models [26, 27], has been widely used in topology optimization due to its lower computational cost and straightforward implementation with volume constraints. For example, the authors of [19] applied Allen–Cahn-based topology optimization to the design of flexoelectric structures, and demonstrated the robustness of the method in various geometries, boundary conditions, and initial material configurations. In our previous work [28], it was demonstrated that topology optimization based on modified Allen-Cahn equations offered advantages in stable hole nucleation and exhibited independence from initial conditions. Although topology optimization in the phase field framework has the ability to produce clear 0-1 topologies and smooth boundary representations, further investigation into local length scale controls remains largely unexplored.

Beyond the aforementioned studies, skeleton-assisted length scale control has also received significant research attention [9, 29–31]. The skeleton is a region-based shape feature that represents the general form of an object, typically characterized by elements such as two-dimensional (2D) pixels and lines. Zobaer et al. [29] extracted the skeleton by a series of inflection points derived from the density distribution at each design step, taking the divergence of the gradient angles. The heat method [32], developed for skeleton extraction, is rarely used nowadays, as a heat equation is required to be solved at each design step [11]. The thinning algorithm [33], proposed 30 years ago, is now widely used for its straightforward implementation, as it relies solely on image pixels rather than gradient density calculations. Yan et al. [34] used the thinning algorithm to extract the structural skeleton, swept a circular feature (for 2D cases) along this skeleton, and set the density variables within the swept region to 1 to enforce the minimum length scale. However, to the best of our knowledge, such methods have not been introduced into the phase field framework.

Therefore, in this work, we propose a phase field topology optimization with length scale control. On the basis of phase field theory, we will construct an energy functional as the objective of topology optimization that integrates all of the required constraints. Through an augmented Lagrangian method, the extremum of the constructed energy functional can be derived by solving time-dependent Allen-Cahn type equations, yielding the optimal material distribution for topology optimization. That is the main idea of phase field topology optimization. Especially, for length scale control constraints, which are also included in the energy functional, we first extract the desired skeleton using the thinning algorithm based on results from the phase field topology optimization without local length scale control. Then local volume constraints are imposed via a convolution operation $\mathcal{B}_r$ along the extracted skeleton, viewed as constraints of the length scale control. In addition, a geometric fidelity between the desired skeleton and the resultant skeleton at each design step will be penalized to improve the results. We use an operator-splitting-based hybrid numerical method to solve the derived Allen-Cahn type equations. Finally, mechanical, thermal, and thermal-mechanical coupled topology optimization are numerically simulated to verify the practicability of the proposed method. It is noted that, for the thermal-mechanical coupled topology optimization, we also analyze the effect of thermal expansion coefficients on the resulting structures.

This section briefly highlights the background of our work. Section 2 covers the theoretical foundation of phase field-based topology optimization, while Section 3 details the techniques used for minimum length scale control, illustrated through a benchmark problem in mechanical topology optimization. The numerical implementations are elaborated and discussed in Section 4.

Applications of the developed method, extended to thermal-mechanical coupled topology optimization, are presented in Section 5. Finally, Section 6 concludes this work by highlighting the key contributions of this study to both the research community and industry.

2. Phase-field based topology optimization

Firstly, we give a brief introduction to linear elasticity. Let $\mathbf{u}$ represent the displacement vector. The strain tensor can be defined as $\nabla^s \mathbf{u} = \frac{1}{2}\left(\nabla \mathbf{u} + (\nabla \mathbf{u})^T\right)$. The strain energy is defined as $w(\phi, \nabla^s \mathbf{u}) = \frac{1}{2}\nabla^s \mathbf{u} : \mathbf{D} : \nabla^s \mathbf{u}$. $\mathbf{D}$ is the fourth-order stiffness tensor. The stress tensor can be defined as $\sigma = w_{,\nabla^s \mathbf{u}}$, where $[\cdot]_{,\mathbf{x}}$ represents a partial differentiation with respect to $\mathbf{x}$, i.e., $\sigma = w_{,\nabla^s \mathbf{u}} = \mathbf{D} : \nabla^s \mathbf{u}$. The equilibrium equation in direct tensor form can be expressed as

$$\mathbf{q} = \nabla \cdot \sigma, \quad \mathbf{x} \in \Omega. \tag{2.1a}$$

$$\mathbf{u} = \mathbf{0}, \quad \text{along } \partial\Omega_u. \tag{2.1b}$$

$$\mathbf{t} = \tilde{\mathbf{t}}, \quad \text{along } \partial\Omega_t. \tag{2.1c}$$

In this work, based on finite element analysis (FEA), we only consider the elastostatics where the displacements are not a function of time and all forces on the elastic body sum to zero. Thus, we assume the elastic body force $\mathbf{q} = \mathbf{0}$ and the traction force $\mathbf{t} = \sigma \cdot \mathbf{n}$. The maximum stiffness, a benchmark problem in topology optimization [35], is considered throughout this work. Because the maximum stiffness is equivalent to the minimum compliance, the objective of topology optimization is expressed as follows:

$$C = \int_{\partial\Omega_t} \tilde{\mathbf{t}} \cdot \mathbf{u} \, dS = \int_{\Omega} \nabla^s \mathbf{u} \cdot \sigma \, dV, \tag{2.2}$$

which is expressed equivalently as the minimization of strain energy,

$$C = \int_{\Omega} 2w(\phi, \nabla^s \mathbf{u}) \, dV. \tag{2.3}$$

Here, $\phi \in [0, 1]$ represents the design variable or the dense variable. Let $\mathbf{D}^0$ represent the fourth-order stiffness tensor of a material, i.e., $\mathbf{D}^0_{ijmn} = \frac{E}{1+\nu}\left(\delta_{im}\delta_{jn} + \frac{\nu}{1-2\nu}\delta_{ij}\delta_{mn}\right)$, where E, ν, and δ are Young's module, the Poisson ratio, and Kronecker delta, respectively. Let $\mathbf{D}$ represent the effective stiffness tensor, which is denoted as $\mathbf{D} = g(\phi)\mathbf{D}^0$. $g(\phi) = \phi^3$ is denoted as the residual stiffness function. Therefore, a general mathematical model of topology optimization can be expressed as follows:

$$\min_{\phi \in [0,1]} \int_{\Omega} 2w(\phi, \nabla^s \mathbf{u}) \, dV$$
$$s.t. \begin{cases} \mathbf{0} = \nabla \cdot \sigma, & \text{in } \Omega, \\ \int_{\Omega} \phi \, dV = V_0, \end{cases} \tag{2.4}$$

with the boundary conditions (2.1b) and (2.1c). V_0 is the constraint on the material volume ratio. As we know, different topology optimization methods use different optimizers to seek for the optimal

design [36]. In the phase-field based topology optimization, the optimal design is transformed into solving PDEs and no additional optimizers are required. To derive such PDEs, a surface free energy functional is introduced to the original objective, that is

$$\mathcal{E}(\phi, \mathbf{u}) = \int_\Omega \left(F(\phi) + \frac{1}{2}\epsilon^2 \|\nabla\phi\|^2 \right) dV + \eta \int_\Omega 2w(\phi, \nabla^s\mathbf{u}) \, dV, \tag{2.5}$$

where $F(\phi) = \frac{1}{4}\phi^2(1-\phi)^2$ represents the double-well potential, which favors a design consisting of regions of either $\phi = 1$ or $\phi = 0$. $\|\nabla\phi\|^2$ results in the transition regions $\phi \in [0, 1]$ being penalized. ϵ, η are constant parameters that reflect the influence of interfacial energy and strain energy on the optimal design. Then the equilibrium conditions, traction boundary conditions and volume constraints, as necessary components in topology optimization, are added into the energy functional (2.5). An augmented energy functional is finally constructed as

$$\mathcal{L}(\phi, \mathbf{u}, \lambda^e, \lambda^t, \lambda^{vol}) = \mathcal{E}(\phi, \mathbf{u}) + \int_\Omega \lambda^e \cdot (\nabla \cdot w_{,\nabla^s\mathbf{u}}) \, dV + \int_{\partial\Omega_t} \lambda^t \cdot \left(\tilde{\mathbf{t}} - w_{,\nabla^s\mathbf{u}} \cdot \mathbf{n} \right) dS$$

$$+ \frac{1}{2}\lambda^{vol} \left(\int_\Omega \phi \, dV - V_0 \right)^2. \tag{2.6}$$

The extremums of the energy functional (2.6) can be derived using the augmented Lagrangian method [37, 38]. Here, $\lambda^e, \lambda^t, \lambda^{vol}$ are called Lagrangian multipliers. The volume constraint is regularized by the Moreau–Yosida regularization method [39] which has the advantages of the availability of highly efficient solvers and the induced numerical stability with respect to the mesh size of discretization. To obtain a stationary point for the minimum problem of (2.6), we will derive the first-order variations $\delta\mathcal{L}$ according to the calculus of variations. Here, we list some equivalent formulas as follows, which will be used in the derivation of $\delta\mathcal{L}$. These formulas can be derived by integration by parts and the divergence theorem.

$$\delta \left(\int_\Omega 2\eta w(\phi, \boldsymbol{\varepsilon}) \, dV \right) = \int_\Omega 2\eta w_{,\phi}\delta\phi \, dV + \int_{\partial\Omega} 2\eta w_{,\varepsilon} \cdot \mathbf{n}\delta\mathbf{u} \, dS - \int_\Omega \nabla \cdot 2\eta w_{,\varepsilon}\delta\mathbf{u} \, dV. \tag{2.7a}$$

$$\int_\Omega \lambda^e \cdot (\nabla \cdot w_{,\varepsilon}) \, dV = \int_{\partial\Omega} \mathbf{n} \cdot (\lambda^e \cdot w_{,\varepsilon}) \, dS - \int_\Omega \nabla\lambda^e : w_{,\varepsilon} \, dV. \tag{2.7b}$$

$$\delta \left(\int_\Omega \nabla\lambda^e : w_{,\varepsilon} \, dV \right) = \int_\Omega \nabla\lambda^e : w_{,\phi\varepsilon}\delta\phi \, dV + \int_{\partial\Omega} \nabla\lambda^e : w_{,\varepsilon\varepsilon} \cdot \mathbf{n}\delta\mathbf{u} \, dS$$

$$- \int_\Omega \nabla \cdot (\nabla\lambda^e : w_{,\varepsilon\varepsilon})\delta\mathbf{u} \, dV. \tag{2.7c}$$

$$\delta \left(\int_{\partial\Omega} \mathbf{n} \cdot (\lambda^e \cdot w_{,\varepsilon}) \, dS \right) = \int_{\partial\Omega} \mathbf{n} \cdot \lambda^e \cdot w_{,\phi\varepsilon}\delta\phi \, dS + \int_{\partial\Omega} \mathbf{n} \cdot \lambda^e \cdot w_{,\varepsilon\varepsilon}\delta\boldsymbol{\varepsilon} \, dS. \tag{2.7d}$$

$$\delta \left(\int_{\partial\Omega_t} \lambda^t \cdot \left(\tilde{\mathbf{t}} - w_{,\varepsilon} \cdot \mathbf{n} \right) dS \right) = -\int_{\partial\Omega_t} \lambda^t \cdot w_{,\phi\varepsilon} \cdot \mathbf{n}\delta\phi \, dS - \int_{\partial\Omega_t} \lambda^t \cdot w_{,\varepsilon\varepsilon} \cdot \mathbf{n}\delta\boldsymbol{\varepsilon} \, dS. \tag{2.7e}$$

Here, two notations $A(\phi) = \int_\Omega \phi \, dV$ and $\boldsymbol{\varepsilon} = \nabla^s\mathbf{u}$ are used. On the basis of the equality formulations mentioned above, for a stationary point to the minimum problem of (2.6) with respect to $\phi, \mathbf{u}, \lambda^e, \lambda^t, \lambda^{vol}$, we derive

$$\delta\mathcal{L} = \int_\Omega \left(F_{,\phi} - \epsilon^2\Delta\phi + 2\eta w_{,\phi} - \nabla\lambda^e : w_{,\varepsilon\phi} + \lambda^{vol}(A(\phi) - V_0) \right)\delta\phi \, dV + \int_{\partial\Omega} \nabla\phi \cdot \mathbf{n}\delta\phi \, dS$$

$$+ \int_{\partial\Omega_t} \left(\lambda^e - \lambda^t\right) \cdot w_{,\varepsilon\phi} \cdot \mathbf{n}\delta\phi \, dS + \int_{\partial\Omega\setminus\partial\Omega_t} \lambda^e w_{,\varepsilon\phi} \cdot \mathbf{n}\delta\phi \, dS$$

$$+ \int_{\partial\Omega} \mathbf{n} \cdot (2\eta w_{,\varepsilon} - \nabla\lambda^e : w_{,\varepsilon\varepsilon}) \cdot \delta\mathbf{u} \, dV$$

$$+ \int_{\Omega} \nabla \cdot (\nabla\lambda^e : w_{,\varepsilon\varepsilon} - 2\eta w_{,\varepsilon}) \, \delta\mathbf{u} \, dV + \int_{\partial\Omega_t} \left(\lambda^e - \lambda^t\right) \cdot (w_{,\varepsilon\varepsilon} : \delta\varepsilon) \cdot \mathbf{n} \, dS$$

$$+ \int_{\partial\Omega\setminus\partial\Omega_t} \lambda^e \cdot (w_{,\varepsilon\varepsilon} : \delta\varepsilon) \cdot \mathbf{n} \, dS. \tag{2.8}$$

Therefore, a stationary point to the extremum of the functional (2.6) is characterized by

$$F_{,\phi} - \epsilon^2 \Delta\phi + 2\eta w_{,\phi} - \nabla\lambda^e : w_{,\varepsilon\phi} + \lambda^{vol}A(\phi) = \lambda^{vol}V_0, \quad \mathbf{x} \in \Omega. \tag{2.9a}$$

$$\mathbf{0} = \nabla \cdot (2\eta w_{,\varepsilon} - \nabla\lambda^e : w_{,\varepsilon\varepsilon}), \quad \mathbf{x} \in \Omega. \tag{2.9b}$$

$$\mathbf{0} = \mathbf{n} \cdot (2\eta w_{,\varepsilon} - \nabla\lambda^e : w_{,\varepsilon\varepsilon}), \quad \text{along } \partial\Omega. \tag{2.9c}$$

$$\lambda^e = \lambda^t, \quad \text{along } \partial\Omega_t. \tag{2.9d}$$

$$\lambda^e = \mathbf{0}, \quad \text{along } (\partial\Omega \setminus \partial\Omega_t) \supset \partial\Omega_u. \tag{2.9e}$$

$$0 = \nabla\phi \cdot \mathbf{n}, \quad \text{along } \partial\Omega. \tag{2.9f}$$

To fulfill (2.9b)–(2.9c), let $\lambda^e = 2\eta\mathbf{u}$. Since the right side of (2.9a) is always a constant at a stationary point, the left side of (2.9a) must be constant throughout the design space. Using the format of strain energy w and $\lambda^e = 2\eta\mathbf{u}$ together, Eq (2.9a) results in,

$$F_{,\phi} - \epsilon^2 \Delta\phi - 2\eta\frac{g_{,\phi}}{g}w + \lambda^{vol}A(\phi) = \lambda^{vol}V_0, \quad \mathbf{x} \in \Omega. \tag{2.10}$$

To solve Eq (2.10), combined with phase field models, we introduce a virtual time with respect to ϕ to find the stationary point of the extremum of the functional (2.6). Thus Eq (2.10) is transformed into the following time-dependent Allen-Cahn type equation:

$$\phi_{,t} = -\frac{1}{\epsilon^2}F_{,\phi} + \Delta\phi + 2\eta\frac{g_{,\phi}}{g}w - \lambda^{vol}(A(\phi) - V_0), \quad \mathbf{x} \in \Omega. \tag{2.11}$$

Finally, the extremum of the functional (2.6) has been transformed into the solutions of Eq (2.11) subject to Eqs (2.1a)–(2.1c) and (2.9f). Since no size control is imposed in this part (designated as skeleton-free topology optimization), the optimal design obtained by Eq (2.11) may not satisfy the minimum length scale required.

3. Topology optimization with a minimum length scale

As the minimum printable size is very important to topology optimization for additive manufacture, we will impose the minimum length scale constraint on the functional (2.6). To achieve that, we first need to define structural skeletons. We use a morphological thinning operation to identify the skeleton. For example, a MATLAB function provided in the MATLAB Image Processing Toolbox can achieve that, i.e., *bwskel*(**A**). Here **A** is a 2D binary image which exactly corresponds to $\phi = 1$ or $\phi = 0$. Its main idea is to iteratively remove pixels on the boundaries of objects and preserve the object's

topology by breaking it into parts. It is noted that other techniques for skeleton extraction [40] can also be applied. We will use ψ to denote the skeleton extracted from the object, that is $\psi = bwskel(\phi)$. Let ψ_0 represent the skeleton extracted from the optimal structure obtained by Eq (2.11), where no size control is imposed. We use $\Xi \subset \Omega$ to represent the gray pixel elements composed of the "skeleton" shown in Figure 1. Next, a moving average operator is defined as follows to represent the average values of the data sets which are included in a circle or a semicircle on the boundary (centered on the point sets in Ξ with a radius of r) as shown in Figure 1.

$$(\mathcal{B}_r * \phi)(\mathbf{x}) = \int_\Omega \mathcal{B}_r(\mathbf{y})\phi(\mathbf{x} - \mathbf{y})\, d\mathbf{y}. \tag{3.1}$$
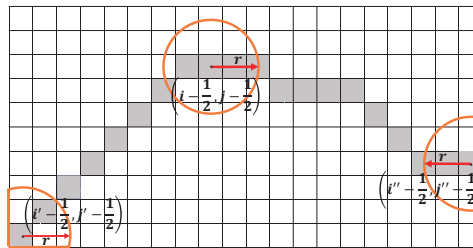

Figure 1. Schematics of the moving average along the extracted "skeleton" (gray pixels).

In order to satisfy the minimum length scale constraint, $\mathcal{B}_r * \phi = 1$ should always be ensured during topology optimization. At the same time, the new structural skeleton ψ is expected to closely approximate the original skeleton ψ_0. These requirements can be fulfilled by adding two regularization terms to the functional (2.6), i.e., $|\mathcal{B}_r * \phi - 1|^2$ and $|\psi - \psi_0|^2$. Thus, we construct a new augmented functional including the minimum length scale constraints as follows:

$$\tilde{\mathcal{L}}(\phi, \mathbf{u}, \lambda^e, \lambda^t, \lambda^{vol}, \lambda^{ske}, \lambda^{\mathcal{B}_r}) = \mathcal{E}(\phi, \mathbf{u}) + \int_\Omega \lambda^e \cdot (\nabla \cdot w_{,\nabla^s \mathbf{u}})\, dV + \int_{\partial\Omega_t} \lambda^t \cdot \left(\tilde{\mathbf{t}} - w_{,\nabla^s \mathbf{u}} \cdot \mathbf{n}\right) dS$$

$$+ \frac{1}{2}\lambda^{vol}\left(\int_\Omega \phi\, dV - V_0\right)^2 + \frac{1}{2}\lambda^{ske}\int_\Omega |\psi - \psi_0|^2\, d\mathbf{x} + \frac{1}{2}\lambda^{\mathcal{B}_r}\int_\Omega |\mathcal{B}_r * \phi - 1|^2\, d\mathbf{x}. \tag{3.2}$$

Here, λ^{ske} and $\lambda^{\mathcal{B}_r}$ are Lagrangian multipliers. To search for a stationary point of the extremum of the functional (3.2), similar to Section 2, the following equations are derived:

$$\phi_{,t} = -F_{,\phi} + \epsilon^2\Delta\phi + 2\eta w_{,\phi} - \lambda^{vol}(A(\phi) - V_0) - \lambda^{ske}(\psi - \psi_0) - \lambda^{\mathcal{B}_r}(\tilde{\phi} - 1), \quad \mathbf{x} \in \Omega. \tag{3.3a}$$

$$\mathbf{0} = \nabla \cdot \sigma, \quad \mathbf{x} \in \Omega. \tag{3.3b}$$

$$\mathbf{0} = \mathbf{n} \cdot \sigma, \quad \text{along } \partial\Omega \setminus \partial\Omega_t. \tag{3.3c}$$

$$\tilde{\mathbf{t}} = \mathbf{n} \cdot \sigma, \quad \text{along } \partial\Omega_t. \tag{3.3d}$$

$$0 = \mathbf{u}, \quad \text{along } \partial\Omega_u. \tag{3.3e}$$

$$0 = \mathbf{n} \cdot \nabla\phi, \quad \text{along } \partial\Omega. \tag{3.3f}$$

Here, $\tilde{\phi} = \mathcal{B}_r * \phi$. According to the derived phase field model (3.3), the topology optimization with the minimum length scale does not require additional optimality criteria and post-processing operations. The flowchart of the proposed method is exhibited in Figure 2.
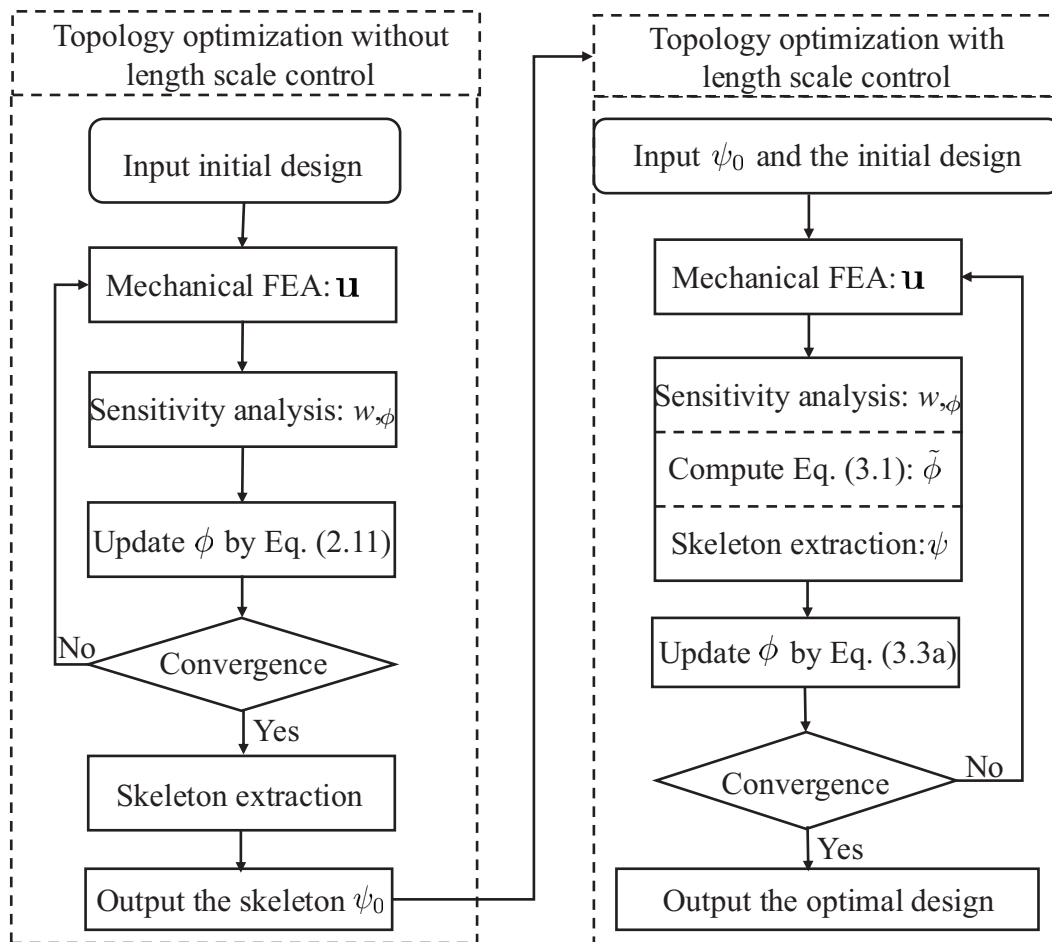
Figure 2. The flowchart of the proposed topology optimization method.

4. Numerical scheme

In the part relating to numerical schemes, the following notations will be used. The computational domain is represented as $\Omega = (0, L_x) \times (0, L_y)$. The unit mesh size is represented as $h = L_x/N_x = L_y/N_y$, with N_x and N_y being positive even integers. We assume that $0 = t^0 < t^1 < \cdots < t^{\mathcal{N}} = T$ and the time step $\Delta t = t^n - t^{n-1}$, $n = 1, 2, \ldots, \mathcal{N}$. T is the total evolution time. We use $\phi_{i,j}^n$ to represent the design variables at the time $n\Delta t$ and the location (i, j), $i = 1, \ldots, N_x$, $j = 1, \ldots, N_y$. A fast algorithm combining with an operator splitting-based hybrid numerical method [41–43] is used to solve Eq (3.3a), which is divided into a series of simpler problems.

$$\mathbf{0} = \nabla \cdot w_{,\varepsilon}(\phi^n, \mathbf{u}^n), \quad \phi^n = \phi(\mathbf{x}, n\Delta t), \tag{4.1a}$$

$$\phi_{,t}^{\mathbf{1}}(\mathbf{x}, t) = -\lambda^{ske}(\psi(\mathbf{x}, t) - \psi_0(\mathbf{x})) - \lambda^{\mathcal{B}_r}(\tilde{\phi}(\mathbf{x}, t) - 1), \quad n\Delta t < t \le (n + 1)\Delta t, \tag{4.1b}$$

$$\phi_{,t}^{\mathbf{2}}(\mathbf{x}, t) = \epsilon^2 \Delta \phi^{\mathbf{1}}(\mathbf{x}, t) - \lambda^{vol}(A(\phi^{\mathbf{1}}(\mathbf{x}, t)) - V_0) + 2\eta \bar{w}(\phi^n, \mathbf{u}^n), \quad n\Delta t < t \le (n + 1)\Delta t, \tag{4.1c}$$

$$\phi_{,t}^{\mathbf{3}}(\mathbf{x}, t) = -F_{,\phi}(\phi^{\mathbf{3}}), \quad n\Delta t < t \le (n + 1)\Delta t. \tag{4.1d}$$

Here, $\mathbf{u}^n$ represents the state variable $\mathbf{u}$ updated by the transient variable ϕ^n, and ψ in (4.1b) represents the extracted skeleton based on ϕ^n, i.e. $\psi = bwskel(\phi^n)$. We use notations $\tilde{\phi} = \mathcal{B}_r * \phi^n$ and $w_{,\phi} = \bar{w}$ for simplicity. The notations ϕ^1, ϕ^2, and ϕ^3 are used to present the solutions of Eqs (4.1b)–(4.1d).

$$
\begin{cases}
\phi^1(\mathbf{x}, n\Delta t) = \phi(\mathbf{x}, n\Delta t), \\
\phi^2(\mathbf{x}, n\Delta t) = \phi^1(\mathbf{x}, (n+1)\Delta t), \\
\phi^3(\mathbf{x}, n\Delta t) = \phi^2(\mathbf{x}, (n+1)\Delta t).
\end{cases}
\tag{4.2}
$$

Thus, the solution of the system (3.3) at time $(n+1)\Delta t$ is $\phi^{n+1} = \phi^3(\mathbf{x}, (n+1)\Delta t)$, and $\mathbf{u}^{n+1}$ can be further updated by $\mathbf{0} = \nabla \cdot w_{,\varepsilon}(\phi^n, \mathbf{u}^{n+1})$. The specified calculation process is as follows. First, given an initial condition ϕ^n, by solving Eq (4.1a) with the boundary conditions (3.3c)–(3.3e), we can obtain $\mathbf{u}^n$. Then we extract the skeleton based on ϕ^n and compute $\tilde{\phi}$ via **Algorithm** 1.

Algorithm 1 Moving average operations

Input: $\psi_0, \phi^n, r, N_x, N_y$
Output: $\tilde{\phi}$

1: [row,col] = find(ψ_0); ▷ find($\cdot$) returns the row and column subscripts of each nonzero element
2: lists = [row,col];
3: $\tilde{\phi}$=zeros(length(ϕ^n));
4: **for** k = 1:length(lists) **do**
5:    indes = lists(k,:);
6:    $r_{vol} = 1$;
7:    $r_{num} = 1$;
8:    **for** i = 1:N_x **do**
9:       **for** j = 1:N_y **do**
10:          $d = \sqrt{(i - \text{lists(k, 1)})^2 + (j - \text{lists(k, 2)})^2}$;
11:          **if** $d <= r$ **then**
12:             $r_{num} = r_{num} + 1$;
13:             **if** $\phi^n(i, j) < 0.999$ **then**
14:                $\phi^n(i, j) = 1$;
15:             **end if**
16:             $r_{vol} = r_{vol} + \phi^n(i, j)$;
17:          **end if**
18:       **end for**
19:    **end for**
20:    $\tilde{\phi}$(indes) = r_{vol}/r_{num};
21: **end for**
22: **return** $\tilde{\phi}$

On the basis of $\phi_{ij}^{1,n+1}$ in Eq (4.1b), we propose the following semi-implicit scheme for Eq (4.1c) to solve $\phi_{ij}^{2,n+1}$,

$$
\frac{\phi_{ij}^{2,n+1} - \phi_{ij}^{1,n+1}}{\Delta t} = \Delta_d \phi_{ij}^{2,n+1} - \lambda^{vol}(A_d(\phi_{ij}^{1,n+1}) - V_0) + 2\eta\bar{w}(\phi_{ij}^n, \mathbf{u}^n).
\tag{4.3}
$$

Here, Δ_d represents the discrete Laplace operator, and $A_d(\phi_{ij}) = \sum_{i,j} \phi_{ij} h^2$. The boundary condition (3.3f) is applied. Let us rewrite Eq (4.1d) as

$$
0 = \mathrm{d}t + \frac{\mathrm{d}\phi}{F_{,\phi}} = \mathrm{d}t + \frac{2\,\mathrm{d}\phi}{\phi} - \frac{2\,\mathrm{d}\phi}{1 - \phi} + \frac{4\,\mathrm{d}\phi}{0.5 - \phi},
\tag{4.4}
$$

which is an ordinary differential equation. With the initial conditions $\phi_{ij}^{2,n+1}$, we solve $\phi_{ij}^{3,n+1}$ as follows:

$$
\phi_{ij}^{3,n+1} = \frac{1}{2} + \frac{\phi_{ij}^{2,n+1} - 0.5}{\sqrt{\exp^{-\Delta t/2} + (2\phi_{ij}^{2,n+1} - 1)^2(1 - \exp^{-\Delta t/2})}}.
\tag{4.5}
$$

Finally, we can obtain the numerical solutions ϕ^{n+1} of the system (3.3) as follows:

$$\phi_{ij}^{n+1} = \phi_{ij}^{3,n+1}. \tag{4.6}$$

Here, $\mathbf{u}^{n+1}$ can be obtained according to the following constitutive equation:

$$\nabla \cdot w_{,\varepsilon}(\phi^{n+1}, \mathbf{u}^{n+1}) = \mathbf{0}. \tag{4.7}$$

5. Numerical examples

In this section, the effectiveness of the proposed method is verified with the examples of a cantilever beam, heat transfer, and a thermal-elastic structure. The corresponding schematics of these structures are listed in Figure 3. For all numerical examples, the fixed mesh of the four-node bilinear square solid element is used to discretize the design domains in 2D problems.

(a) (b) (c)
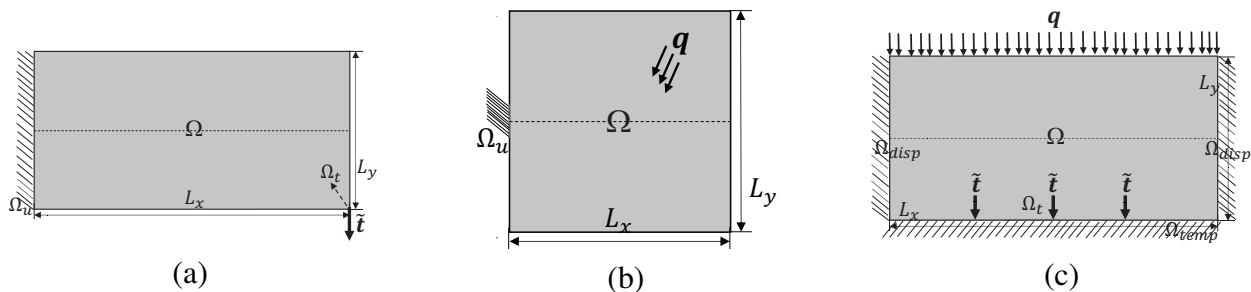
Figure 3. (a) Schematic of the cantilever beam; (b) schematic of heat transfer; (c) schematic of the thermal-elastic structures.

5.1. Mechanical topology optimization

The first example is a cantilever beam problem, shown in Fig. 3(a). The design domain $\Omega = [0, L_x] \times [0, L_y]$ is discretized by the 200×100 meshgrid with $L_x = 10, L_y = 5$ and $h = 0.05$. The traction force $\mathbf{t} = [0, -1]$ is loaded on the lower right corner. The other sides satisfies $\sigma \cdot \mathbf{n} = \mathbf{0}$. The left side is fixed, i.e. $\mathbf{u} = 0$. An isotropic material with the elastic modulus $E = 1$ and the Poisson ratio $\nu = 0.3$ is used here. Assume that the predefined material volume ratio V_0 is 0.3. The initial configurations are $\phi^0 = V_0$, and the Neumann boundary condition for ϕ is adopted. The parameters included in the proposed numerical schemes are set as $\{\Delta t, T, \epsilon, \eta, \lambda^{vol}, \lambda^{ske}, \lambda^{\mathcal{B}_r}, r_{\min}\} = \{0.01, 4, 1 \setminus (\sqrt{2}\tanh^{-1}(0.9)), 0.5, 100, 0.5, 1.0, 3h\}$.

The picture marked as 'skeleton-free' in Figure 4 is the result of the skeleton-free topology optimization. Then we extract the structural skeleton and dilate the structure via the proposed size control method, as shown in Figure 4(a). It is noted that the optimized beam in Figure 4(a) exhibits a discontinuous rib in the bottom right region after imposing the minimum length scale on the beam of the 'skeleton-free' topology. This anomaly is a consequence of the boundary limitation or the non-uniformity of the filtering operation in the boundary regions during optimization. This matter is of particular importance for stress-constrained topology optimization, since the maximum stress is likely to occur at the design domain boundary, which has evolved into a research topic in topology optimization [44, 45] as a remedy operation. To mitigate the boundary effects and provide

a clearer picture of how the length scale constraints impact the performance and manufacturability, we use padding techniques [45] to expand the design region before performing topology optimization with minimum length scale control. In Figure 4(b), the spurious branches of the skeleton extracted from 'skeleton-free' structure have been pruned and padded, yielding the optimized structure via the proposed topology optimization with minimum length scale control. Comparing the 'skeleton-free' structure with the optimized structure in Figure 4(b), we can observe that the lower right part of the beam has obviously been dilated, which verified the effectiveness of our proposed method. Figure 4(c),(d) depicts the curves of structural compliance and volume changes during the optimization process of the 'skeleton-free' structure and the skeleton-assisted structure in Figure 4(b). It is indicated that there is a potential trade-off: While the minimum length scale constraint with padding ensures a more robust and connected design, although it might sacrifice local design intricacies that could be crucial to minimizing the compliance. From Figure 4(d), we can see that the volume constraints are always satisfied for both the skeleton-free and skeleton-assisted methods.
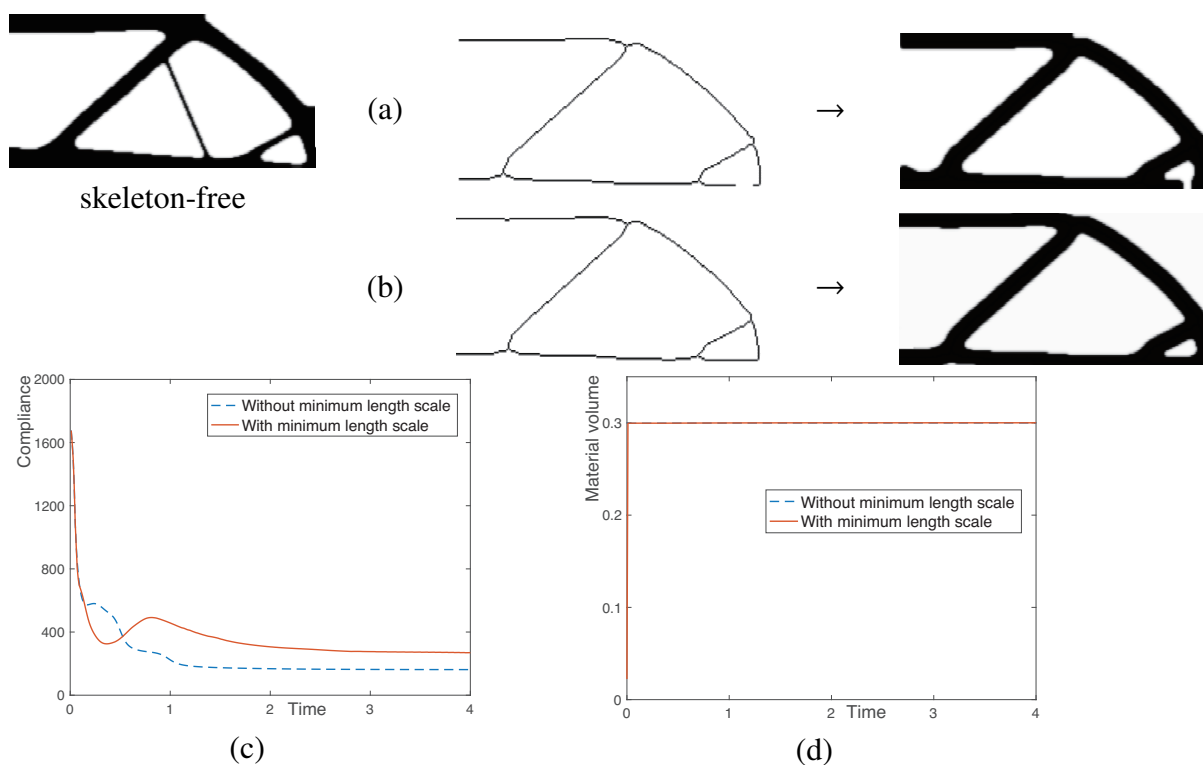

Figure 4. The top left corner ('skeleton-free') is the result of topology optimization without a minimum length scale constraint; (a) the result with minimum length scale constraint based on the extracted skeleton of the 'skeleton-free' method; (b) the result with the minimum length scale constraint and padding techniques [45] based on the extracted skeleton of the 'skeleton-free' method after pruning and padding; (c) the structural compliance history for the optimization process of the 'skeleton-free' method and (b); (d) the volume ratio history for the optimization process of the 'skeleton-free' method and (b).

5.2. Ablation analysis

It can be difficult for skeleton-based length scale control to calculate the sensitivity of the skeleton. In order to analyze the effectiveness of the proposed method and evaluate the contribution of each constraint to the overall performance, an ablation analysis [46] is performed. For simplicity, the constraints in the functional (3.2) are labeled as I, II, III, and IV as follows.

$$\tilde{\mathcal{L}}(\phi, \mathbf{u}, \lambda^e, \lambda^t, \lambda_1, \lambda_2, \lambda_3) = \int_{\Omega} 2\eta w(\phi, \nabla^s \mathbf{u}) \, d\mathbf{x} + \int_{\Omega} \lambda^e \cdot (\nabla \cdot w_{,\nabla^s \mathbf{u}}) \, d\mathbf{x} + \int_{\partial\Omega_t} \lambda^t \cdot \left(\tilde{\mathbf{t}} - w_{,\nabla^s \mathbf{u}} \cdot \mathbf{n} \right) dS$$
$$+ \underbrace{\int_{\Omega} F(\phi) \, d\mathbf{x} + \frac{\epsilon^2}{2} \int_{\Omega} \|\nabla\phi\|^2 \, d\mathbf{x}}_{\text{(I)} \qquad \text{(II)}} + \lambda_1 \underbrace{\left| \int_{\Omega} \phi \, dV - V_0 \right|^2}_{} + \lambda_2 \underbrace{\int_{\Omega} |\psi - \psi_0|^2 \, d\mathbf{x}}_{\text{(III)}} + \lambda_3 \underbrace{\int_{\Omega} |\mathcal{B}_r * \phi - 1|^2 \, d\mathbf{x}}_{\text{(IV)}}.$$

The ablation analysis is performed, based on the cantilever beam problem in Section 5.1, the details of which are shown in Table 1. The first column ('Ablations') in Table 1 represents the constraint marked by a capital Roman numeral being removed from the energy functional (3.2). It can be seen from the experimental results that when the minimum length control constraint (marked by IV) is removed, a trade-off emerges between the minimum length scale and compliance; however, there is a local length scale that does not meet the expected performance, such as the boundary of the structure near the bottom of the design region. When the skeleton fidelity term (marked by III) is removed, it is better to run the skeleton-free topology optimization for several iterations until a physically meaningful structure emerges. This is because the thinning algorithm should not be applied to the initial uniform density field directly; otherwise, this would produce disordered, physically meaningless skeletons from the initial guess, hindering the evolution of the structural topology towards its optimum. From Table 1, we can see that when the skeleton's fidelity is removed from the functional (3.2), the mechanical performance decreases, which confirms the importance of the skeleton's fidelity in improving the overall performance of the method. When the double-well potential (marked by I) is removed, the design region can not separate into the two distinct phases of $\phi = 1$ (solid phase) and $\phi = 0$ (void phase). Removing the constraint depending on the gradient of ϕ (marked by II) leads to numerical instabilities in the optimized material layout. Overall, these findings demonstrate the importance of the various constraints in the proposed method working together to achieve the robustness and the optimal performance.

Table 1. Analysis of the performance effects of different constraints in the proposed method.

Ablations	Optim. Struct.	Compliance	Volume
None		299.29	0.3
IV		224.59	0.3
III		372.70	0.3
I		473.12	0.3
II		8286.85	0.3

Note: All schemes stop at 200 iterations.

5.3. Thermal topology optimization

In this example, a classical problem of volume-point heat conduction [47, 48] is dealt with. As shown in Figure 3(b), a square design domain $\Omega = [0, L_x] \times [0, L_y]$ is discretized by the 200×200 meshgrid with $L_x = 1, L_y = 1$, and $h = 0.005$. A uniform heat source $\mathbf{q} = 1$ is imposed throughout the design domain. All boundaries of $\partial\Omega$ are adiabatic, except that the center part $l_0 = [\frac{7}{20}L_y : 2h : \frac{13}{20}L_y]$ of the left side is $\mathbf{u} = 0$. The thermal compliance can be written as,

$$C = \int_\Omega 2w(\phi, \nabla\mathbf{u}) \, \mathrm{d}V = \int_\Omega \nabla\mathbf{u} : g(\phi)\mathbf{I} : \nabla\mathbf{u} \, \mathrm{d}V. \tag{5.1}$$

Here, $\mathbf{I}$ is an identity matrix. According to Section 2 and 3, the following equations can be derived:

$$\phi_{,t} = -F_{,\phi} + \epsilon^2 \Delta\phi + 2\eta w_{,\phi} - \lambda^{vol}(A(\phi) - V_0) - \lambda^{ske}(\psi - \psi_0) - \lambda^{\mathcal{B}_r}(\tilde{\phi} - 1), \quad \mathbf{x} \in \Omega. \tag{5.2a}$$

$$\mathbf{q} = \nabla \cdot (g(\phi)\nabla\mathbf{u}), \quad \mathbf{x} \in \Omega. \tag{5.2b}$$

$$\mathbf{0} = \mathbf{u}, \quad \text{along } \partial\Omega_u. \tag{5.2c}$$

$$\mathbf{0} = \nabla\mathbf{u} \cdot \mathbf{n}, \quad \text{along } \partial\Omega. \tag{5.2d}$$

$$0 = \mathbf{n} \cdot \nabla\phi, \quad \text{along } \partial\Omega. \tag{5.2e}$$

Assume that the predefined volume ratio of the material V_0 is 0.3 and the initial configurations are $\phi^0 = V_0$. The parameters included in the numerical scheme are set as, $\{\Delta t, T, \epsilon, \eta, \lambda^{vol}, \lambda^{ske}, \lambda^{\mathcal{B}_r}, r_{\min}\} = \{0.01, 2, 1 \setminus (\sqrt{2}\tanh^{-1}(0.9)), 0.5, 60, 0.5, 1, 2h\}$.

Figure 5(a) is the result of the skeleton-free topology optimization. We extract the structural skeleton based on Figure 5(a), and the spurious branches of the skeleton extracted by the thinning

algorithm have been pruned, yielding the skeleton as shown in Figure 5(b). Figure 5(c) is the result of the proposed topology optimization with minimum length scale control. It is obvious that the main branches get thicker and most 'spurs' have been pruned with the minimum length scale control being imposed. Figure 5(d) and (e) depicts the changes in thermal compliance and volume ratio between the skeleton-free and skeleton-assisted methods. It can be seen that when the minimum length scale constraint is imposed, the thermal compliance becomes larger than that without size control, while the volume ratio is not affected. This conclusion is consistent with that of mechanical topology optimization, which proves the broad applicability of the proposed method.
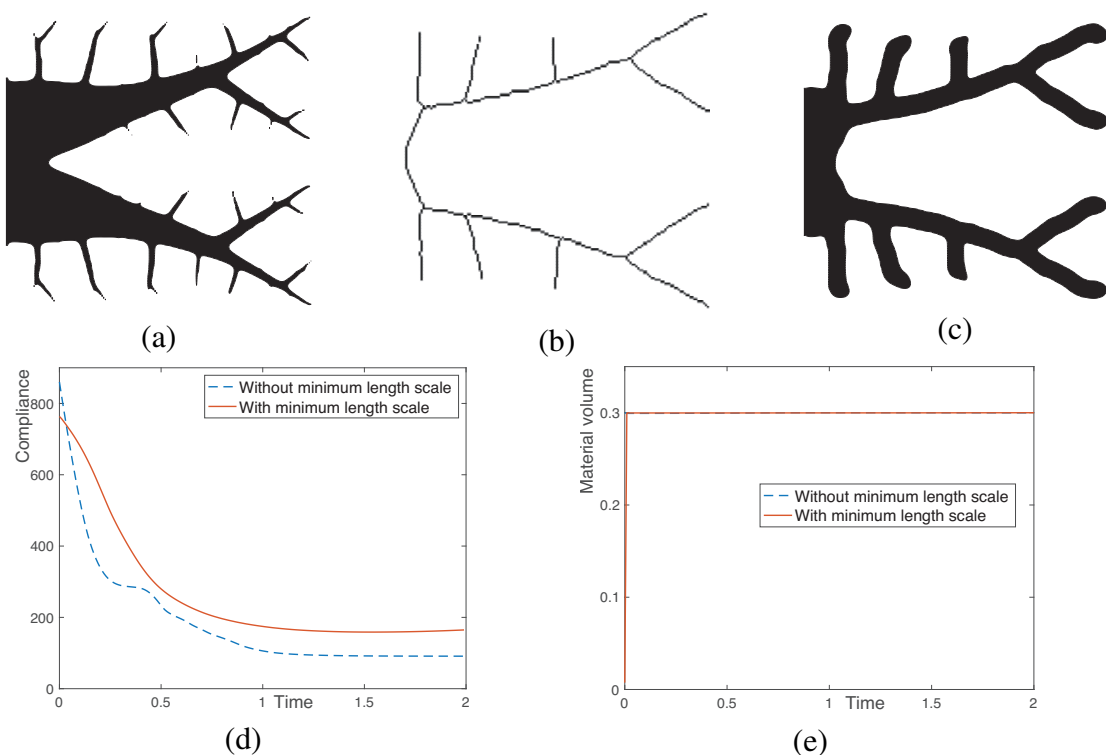

Figure 5. The results of thermal topology optimization: (a) without the minimum length scale constraint; (b) the corresponding extracted skeleton of (a) after pruning; (c) with the minimum length scale constraint; (d) the history of heat compliance; (e) the history of the volume ratio.

To further demonstrate the effectiveness of the method, the algorithm is run with different dilation radii. In Figure 6 (a), the dilation radius is $6h$. In Figure 6 (b), the dilation radius is $4h$. In Figure 6 (c), the dilation radius is $2h$. Other settings remain the same as the optimization case in Figure 5. The objective values obtained in Figure 6 (a)–(c) are 189.42, 187.94, and 184.88, respectively, and the final volume fractions are 0.3190, 0.3088, and 0.2915, respectively. As for the volume fractions, the optimized structures have achieved a unified length scale with predefined radii, demonstrating the effectiveness of the phase-field based topology optimization with length scale control. However, the volume fractions do not reach their target volumes accurately, which is the result of the strong length scale restriction.
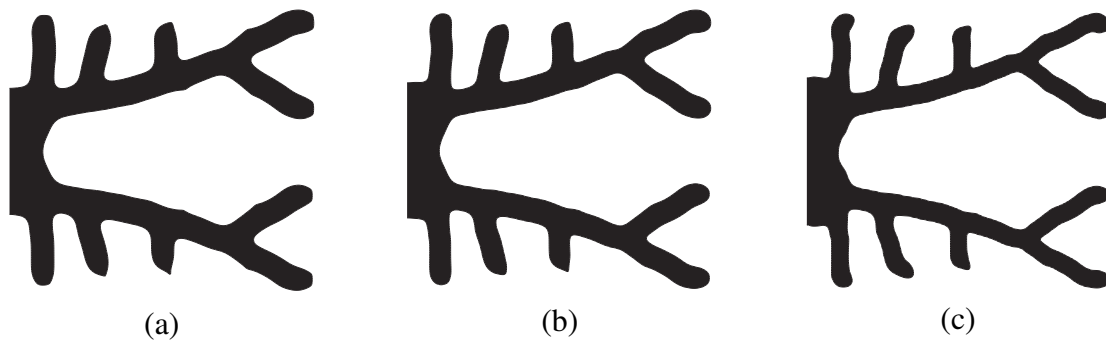
Figure 6. The results of thermal topology optimization with different length scales. From left to right, the length scale target is $6h$, $4h$, and $2h$, respectively.

5.4. Thermal-mechanical coupled topology optimization

In this example, a distributed heat flux is imposed on top of a structure [49, 50] as shown in Fig. 3(c). The boundary condition of heat flux $\mathbf{q} = 1$ is imposed on each node along the top side, and the temperature along the bottom side Ω_{temp} is set to zero as a heat sink. The traction force $\tilde{\mathbf{t}} = [0, -1]$ is loaded on one, two, and three quarters of the bottom side, or along Ω_t . The other sides satisfy $\boldsymbol{\sigma} \cdot \mathbf{n} = \mathbf{0}$. The left and right sides are fixed, i.e. $\mathbf{u} = 0$, along Ω_{disp}. Here, we use the notations $\mathbf{U}$ and $\mathbf{T}$ to distinguish the displacement vector and the temperature variable, respectively. We will compare two conditions, one with thermal expansion of the material, and the other without.

When there is no thermal expansion of the material, the thermal stress on the material is not considered. The total thermal-mechanical compliance, the augmented Lagrangian functional, and the correspondingly derived equations for the extremum of the augmented Lagrangian functional can be expressed as the following, respectively:

$$C = \int_\Omega \Big(2w^{mech}(\phi, \nabla^s\mathbf{U}) + 2w^{heat}(\phi, \nabla\mathbf{T})\Big)\,\mathrm{d}V. \tag{5.3}$$

$$\tilde{\mathcal{L}}(\phi, \mathbf{U}, \lambda_1^e, \lambda_1^t, \lambda_2^e, \lambda_2^t, \lambda^{vol}, \lambda^{ske}, \lambda^{\mathcal{B}_r})$$
$$= \mathcal{E}(\phi, \mathbf{u}) + \int_\Omega \lambda_1^e \cdot \Big(\nabla \cdot w^{mech}{}_{,\nabla^s\mathbf{U}}\Big)\,\mathrm{d}V + \int_\Omega \lambda_2^e \cdot \Big(\nabla \cdot w^{heat}{}_{,\nabla\mathbf{T}}\Big)\,\mathrm{d}V$$
$$+ \int_{\partial\Omega_t} \lambda_1^t \cdot \Big(\tilde{\mathbf{t}} - w^{mech}{}_{,\nabla^s\mathbf{U}} \cdot \mathbf{n}\Big)\,\mathrm{d}S + \int_{\partial\Omega_{disp}} \lambda_2^t \cdot \Big(\mathbf{q} - w^{heat}{}_{,\nabla\mathbf{T}} \cdot \mathbf{n}\Big)\,\mathrm{d}S + \frac{1}{2}\lambda^{vol}\left(\int_\Omega \phi\,\mathrm{d}V - V_0\right)^2$$
$$+ \frac{1}{2}\lambda^{ske}\int_\Omega |\psi - \psi_0|^2\,\mathrm{d}\mathbf{x} + \frac{1}{2}\lambda^{\mathcal{B}_r}\int_\Omega |\mathcal{B}_r * \phi - 1|^2\,\mathrm{d}\mathbf{x}. \tag{5.4}$$

$$\phi_{,t} = -F_{,\phi} + \epsilon^2\Delta\phi + 2\eta^{mech}w^{mech}_{,\phi} + 2\eta^{heat}w^{heat}_{,\phi} - \lambda^{vol}(A(\phi) - V_0) - \lambda^{ske}(\psi - \psi_0)$$
$$- \lambda^{\mathcal{B}_r}(\tilde{\phi} - 1), \quad \mathbf{x} \in \Omega. \tag{5.5a}$$
$$\mathbf{0} = \nabla \cdot \boldsymbol{\sigma}, \quad \mathbf{x} \in \Omega. \tag{5.5b}$$
$$\mathbf{0} = \nabla \cdot (g(\phi)\nabla\mathbf{T}), \quad \mathbf{x} \in \Omega. \tag{5.5c}$$

$$\mathbf{0} = \mathbf{U}, \quad \text{along } \partial\Omega_{disp}. \tag{5.5d}$$

$$\tilde{\mathbf{t}} = \mathbf{n} \cdot \sigma, \quad \text{along } \partial\Omega_{t}. \tag{5.5e}$$

$$\mathbf{q} = \nabla T \cdot \mathbf{n}, \quad \text{along } \partial\Omega_{disp}. \tag{5.5f}$$

$$0 = T, \quad \text{along } \partial\Omega_{temp}. \tag{5.5g}$$

$$\mathbf{0} = \mathbf{n} \cdot \sigma, \quad \text{along } \partial\Omega \setminus \partial\Omega_{t}. \tag{5.5h}$$

$$0 = \nabla T \cdot \mathbf{n}, \quad \text{along } \partial\Omega \setminus \partial\Omega_{disp}. \tag{5.5i}$$

$$0 = \mathbf{n} \cdot \nabla\phi, \quad \text{along } \partial\Omega. \tag{5.5j}$$

If the material is affected by thermal expansion, thermal stress on the material is considered. Then the constitutive equations become,

$$\mathbf{0} = \nabla \cdot \sigma^*, \quad \mathbf{x} \in \Omega. \tag{5.6a}$$

$$\sigma^* = \sigma + \mathbf{D} : \alpha T. \tag{5.6b}$$

Here, α is the linear thermal expansion coefficient $\alpha = [\alpha_{ij}]$. The isotropy of the heat conduction of materials is assumed in this part. For the thermal-mechanical coupled topology optimization with thermal stress, we use Eq (5.6a) to replace Eq (5.5b), and the other equations (5.5c)–(5.5j) remain unchanged. Another significant difference is the sensitivity analysis term included in Eq (5.5a). The details of the related derivation can be found in [49, 50].

The following numerical tests highlight the difference when length scale control is or is not imposed on the two models with and without thermal stress on the materials. The same initial conditions are assumed in the first place. The computational region $\Omega = [0, L_x] \times [0, L_y]$ is discretized by a 240×90 mesh grid with $L_x = 2.4, L_y = 0.9$, and $h = 0.01$. Assume that the predefined material volume ratio V_0 is 0.3 and the initial configuration is $\phi^0 = V_0$. The parameters included in the numerical scheme are set as, $\{\Delta t, T, \epsilon, \eta, \alpha, \lambda^{vol}, \lambda^{ske}, \lambda^{\mathcal{B}_r}, r_{\min}\} = \{0.001, 10, 1 \setminus (\sqrt{2}\tanh^{-1}(0.9)), 0.5, 1, 100, 0.5, 1.0, 3h\}$.

When no size control is considered, the optimal results of the thermal-mechanical coupled topology optimization without thermal stress and with thermal stress are presented in Figure 7. It is obvious that thermal stress on the materials leads to more holes in the optimal shapes, and small features exist when no size control is imposed. Then the thinning algorithm is used to obtain the corresponding skeletons as shown in Figure 8.

When size control is considered, the optimal results of coupled topology optimization with and without thermal stress on the materials are presented in Figure 9. It can be seen that the skeletons have been dilated to some extent. For the coupled topology optimization with thermal stress, the number of holes is greater than that without the thermal stress. In addition, the temperature appears to be lower, which implies that the thermal conductivity of the materials becomes smaller because some heat has been absorbed into the materials. It is noted that Figure 9(c) shows support structures near the left and right corners, which may result in increased fabrication and clean-up costs. The appearance of support structures may be caused by the predefined skeleton, where more holes are created when there is thermal expansion of the materials. To reduce these support structures, the concurrent optimization in topology and length scale control should be studied instead of predefined skeletons. We will verify this conclusion in the next experiment.
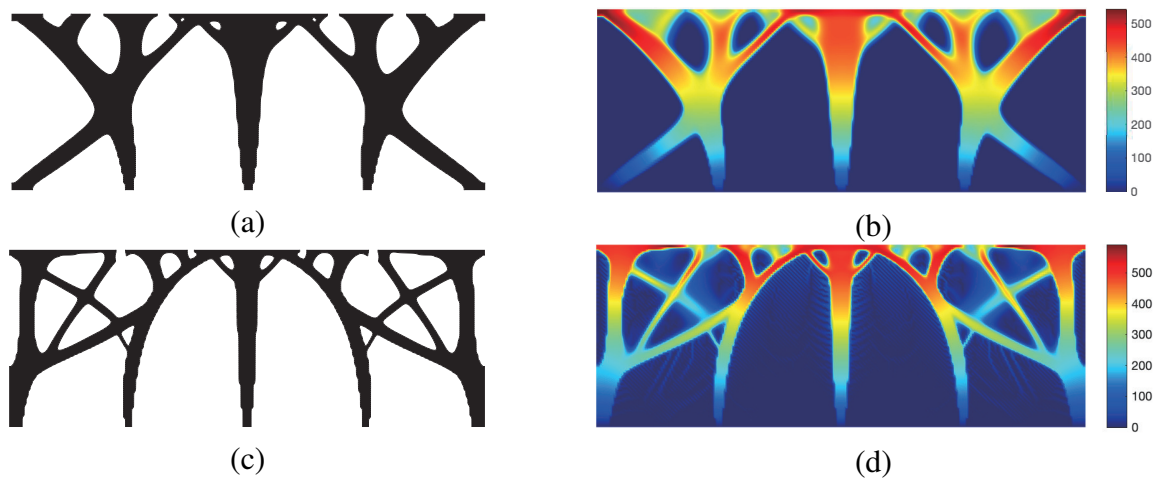
Figure 7. Results of thermal-mechanical coupled topology optimization without the minimum length scale control. (a),(c) The optimal shapes without and with thermal expansion of the materials. (b),(d) The corresponding thermal distribution.

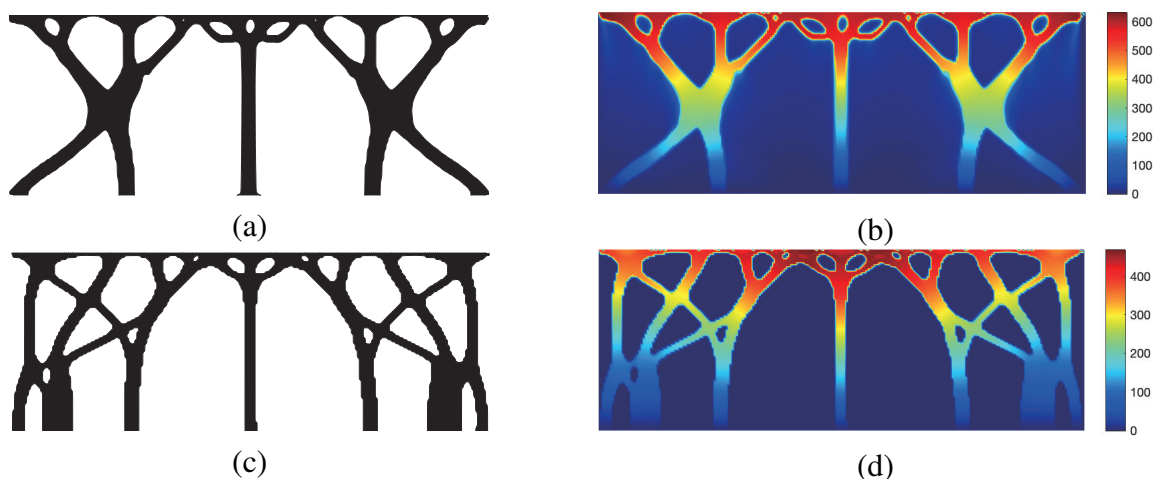**Figure 8.** From left to right: the extracted skeletons from Figure 7(a) and Figure 7 (c).

Figure 9. Results of thermal-mechanical coupled topology optimization with the minimum length scale control. (a),(c) The optimal shapes without and with thermal expansion of the materials. (b),(d) The corresponding thermal distribution.

5.5. Concurrent optimization in topology and length scale control

In this test, the adaptive control of the minimum length scale for thermal-mechanical coupled topology optimization will be proposed to achieve concurrent optimization in topology and length

scale control. The flowchart is exhibited in Figure 10. The main characteristic of this algorithm is that the concurrent method runs the topology optimization without the minimum length scale (i.e., the condition of Eq (2.11) is activated) for a few iterations until a physically meaningful structure develops (i.e., the condition of Eq (3.3a) is activated), and then two conditions occur alternately. The thermal expansion of the materials during the topology optimization coupling of heat and mechanics is considered here. The computation region and the parameters are the same as in Section 5.4. As shown in Figure 11(c), we can see that the adaptive length scale control can avoid support structures, which is beneficial to reduce the fabrication cost. Moreover, as mentioned in Section 1, the Allen-Cahn model has an impact on the perimeter control of holes. Here, we will use different values of η to quantify the effects of the Allen-Cahn model on the optimal designs. When η takes a higher value, the Allen-Cahn model has less effect on perimeter control, leading to a large number of holes. In contrast, when η takes a smaller value, the Allen-Cahn model has a great effect on perimeter control, resulting in fewer holes. The results in Figure 11(a)–(c) confirm this conclusion.
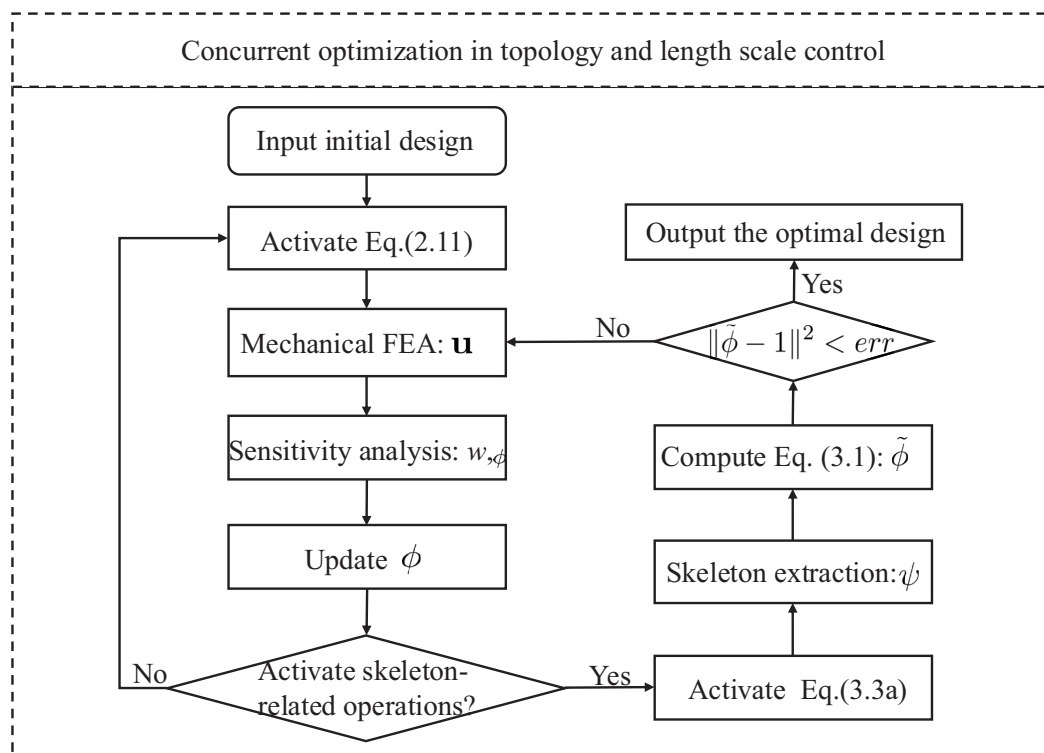

Figure 10. The flowchart of concurrent optimization in topology and length scale control.
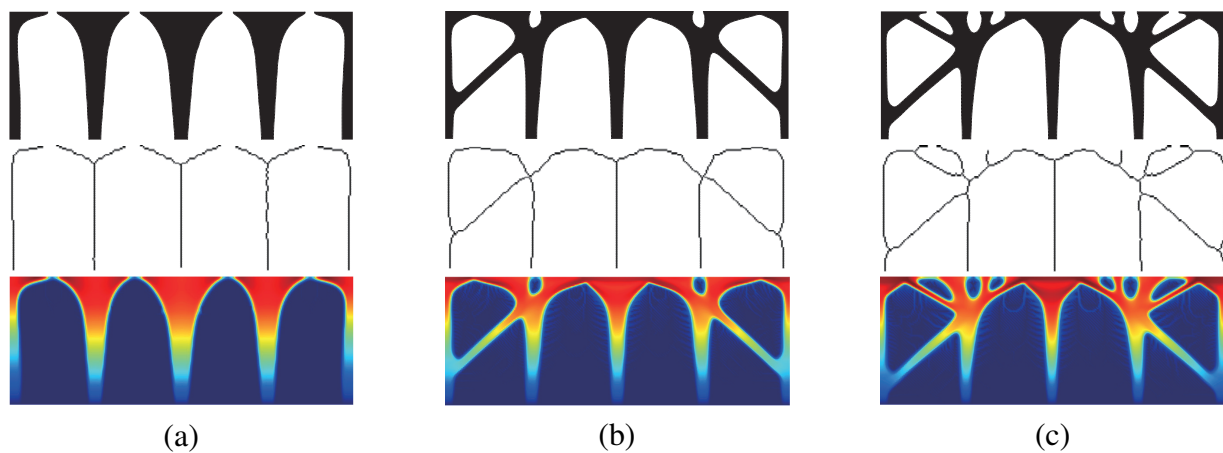
Figure 11. The results of concurrent optimization in topology and size control under different perimeter constraints. (a) $\eta = 0.15$; (b) $\eta = 0.3$; (c) $\eta = 0.5$.

6. Conclusions

This paper presents a phase-field-based topology optimization method that enables minimum length scale control, which can be extended to topology optimization with multi-physics coupling fields. The main idea of this method is to reconstruct a multi-objective functional with volume constraint, size control constraint, and skeleton regularization as a new energy functional of the phase field. By combining an augmented Lagrangian approach and phase field theory, the problem of topology optimization with size control is reformulated into solving Allen-Cahn type equations. An operator splitting numerical scheme is proposed to solve these equations. The numerical results demonstrated that, for both thermal and mechanical compliance minimization problems, the proposed method effectively enforced size constraints; however, a trade-off was observed between size control and the resulting compliance. Ablation analysis was studied to validate the contributions of each component of the proposed method. The double-well potential and the gradient-related term in the phase field model indeed regularize the topology optimization problem. The influence of the radii related to length scale control on the optimized configurations was discussed to demonstrate the effectiveness of the method. In the thermal-mechanical coupled topology optimization, we found that thermal stress in the materials tended to promote the formation of additional holes. We also verified that the perimeters of these holes could be controlled by the derived Allen-Cahn type equations, which had a significant effect on the structural length scale. At the end of this work, we demonstrated that the proposed adaptive size control method improved designs with reduced support structures.

In future work, the derivable sensitivity of the skeleton and the boundary limitation problem will be explored, based on the proposed method. The effect of length scale control on standard benchmark problems has room to improve if the maximum overhang angle, another critical technique for additive manufacturing, is further considered. The algorithm proposed in this study can also be extended to three-dimensional(3D) applications. In such cases, the convolution operation of $\mathcal{B}_r$ will be applied along the skeleton using spherical regions. Future works will focus on discussing methods to address the limitations mentioned above and enhance the current approach to better design 3D structures.

Use of Generative AI tools declaration

The authors declare they have not used artificial intelligence (AI) tools in the creation of this article.

Author contributions

Qian Yu: Conceptualization, methodology, software, writing—original draft, writing—review and editing; Yuyan Liu: Visualization; Mingyuan Yang: Software, writing—review and editing, supervision. All authors have read and approved the published version of the manuscript.

Acknowledgments

Conflict of interest

The authors declare no conflicts of interest in this paper.

References

1. J. Pellens, G. Lombaert, B. Lazarov, M. Schevenels, Combined length scale and overhang angle control in minimum compliance topology optimization for additive manufacturing, *Struct. Multidiscip. O.*, **15** (2019), 2005–2022. https://doi.org/10.1007/s00158-018-2168-z

2. E. Fernández, C. Ayas, M. Langelaar, P. Duysinx, Topology optimisation for large-scale additive manufacturing: generating designs tailored to the deposition nozzle size, *Virtual Phys. Prototyp.*, **16** (2021), 196–220. https://doi.org/10.1080/17452759.2021.1914893

3. Z. Li, L. Wang, T. Lv, Additive manufacturing-oriented concurrent robust topology optimization considering size control, *Int. J. Mech. Sci.*, **250** (2023), 108269. https://doi.org/10.1016/j.ijmecsci.2023.108269

4. R. L. Cortez, M. Setta, R. Picelli, E. Wadbro, Minimum size control for binary topology optimization, *Struct. Multidiscip. O.*, **68** (2025). https://doi.org/10.1007/s00158-025-03975-3

5. W. Zhang, W. Zhong, X. Guo, An explicit length scale control approach in SIMP-based topology optimization, *Comput. Method. Appl. M.*, **282** (2014), 71–86. https://doi.org/10.1016/j.cma.2014.08.027

6. H. Azegami, S. Kaizu, K. Takeuchi, Regular solution to topology optimization problems of continua, *JSIAM Lett.*, **3** (2011), 1–4. https://doi.org/10.14495/jsiaml.3.1

7. O. Sigmund, J. Petersson, Numerical instabilities in topology optimization: A survey on procedures dealing with checkerboards, mesh-dependencies and local minima, *Struct. Optimization*, **16** (1998), 68–75. https://doi.org/10.1007/BF01214002

8. T. Borrvall, J. Petersson, Topology optimization using regularized intermediate density control, *Comput. Method. Appl. M.*, **190** (2001), 4911–4928. https://doi.org/10.1016/S0045-7825(00)00356-X

9. Q. Li, G. Liang, Y. Luo, F. Zhang, S. Liu, An explicit formulation for minimum length scale control in density-based topology optimization, *Comput. Method. Appl. M.*, **404** (2023), 115761. https://doi.org/10.1016/j.cma.2022.115761

10. L. Song, J. Zhao, T. Gao, J. Li, L. Tang, Y. Li, et al., Length scale control in density-based multi-material topology optimization, *Comput. Method. Appl. M.*, **401** (2022), 115655. https://doi.org/10.1016/j.cma.2022.115655

11. J. Huang, J. Liu, Derivable skeletons in topology optimization for length scale control, *Comput. Method. Appl. M.*, **421** (2024), 116778. https://doi.org/10.1016/j.cma.2024.116778

12. M. Jansen, Explicit level set and density methods for topology optimization with equivalent minimum length scale constraints, *Struct. Multidiscip. O.*, **59** (2019), 1775–1788. https://doi.org/10.1007/s00158-018-2162-5

13. J. L. Barrera, M. J. Geiss, K. Maute, Minimum feature size control in level set topology optimization via density fields, *Struct. Multidiscip. O.*, **65** (2022). https://doi.org/10.1007/s00158-021-03096-7

14. Y. Wang, T. Hu, Z. Zou, Y. Wang, X. Zhang, Constraint-free length scale control for topology optimization using the velocity field level set method, *Struct. Multidiscip. O.*, **68** (2025). https://doi.org/10.1007/s00158-025-03971-7

15. J. L. Barrera, M. J. Geiss, K. Maute, Hole seeding in level set topology optimization via density fields, *Struct. Multidiscpip. O.*, **61** (2020), 1319–1343. https://doi.org/10.1007/s00158-019-02480-8

16. M. Zhou, B. Lazarov, F. Wang, O. Sigmund, Minimum length scale in topology optimization by geometric constraints, *Comput. Methods Appl. Mech. Eng.*, **293** (2015), 266–282. https://doi.org/10.1016/j.cma.2015.05.003

17. L. Zhou, T. Gao, W. Zhang, Hole control methods in feature-driven topology optimization, *Comput. Method. Appl. M.*, **417** (2023), 116447. https://doi.org/10.1016/j.cma.2023.116447

18. A. Takezawa, S. Nishiwaki, M. Kitamura, Shape and topology optimization based on the phase field method and sensitivity analysis, *J. Comput. Phys.*, **229** (2010), 2697–2718. https://doi.org/10.1016/j.jcp.2009.12.017

19. J. López, N. Valizadeh, T. Rabczuk, An isogeometric phase-field based shape and topology optimization for flexoelectric structures, *Comput. Method. Appl. M.*, **391** (2022), 114564. https://doi.org/10.1016/j.cma.2021.114564

20. W. Xie, J. Feng, Q. Xia, J. Kim, Y. Li, Design of the shell-infill structures using a phase field-based topology optimization method, *Comput. Method. Appl. M.*, **429** (2024), 117138. https://doi.org/10.1016/j.cma.2024.117138

21. Q. Xia, J. Kim, B. Xia, Y. Li, An unconditionally energy stable method for binary incompressible heat conductive fluids based on the phase–field model, *Comput. Math. Appl.*, **123** (2022), 26–39. https://doi.org/10.1016/j.camwa.2022.07.022

22. D. Cai, B. Fu, R. Gao, X. Kong, J. Yang, Phase-field computation for 3D shell reconstruction with an energy-stable and uniquely solvable BDF2 method, *Comput. Math. Appl.*, **189** (2025), 1–23. https://doi.org/10.1016/j.camwa.2025.03.022

23. O. Sigmund, A 99 line topology optimization code written in Matlab, *Struct. Multidiscip. O.*, **21** (2001), 120–127. https://doi.org/10.1007/s001580050176

24. J. V. Carstensen, J. K. Guest, Projection-based two-phase minimum and maximum length scale control in topology optimization, *Struct. Multidiscip. O.*, **58** (2018), 1845–1860. https://doi.org/10.1007/s00158-018-2066-4

25. R. B. Haber, M. P. Bendose, C. S. Jog, Perimeter constrained topology optimization of continuum structures. In *IUTAM Symposium on Optimization of Mechanical Systems* (eds. D. Bestle and W. Schiehlen), Kluwer Academic Publishers, (1996), 113–120. https://doi.org/10.1007/978-94-009-0153-7_15

26. S. M. Allen, J. W. Cahn, A microscopic theory for antiphase boundary motion and its application to antiphase domain coarsening, *Acta Metall.*, **27** (1979), 1085–1095. https://doi.org/10.1016/0001-6160(79)90196-2

27. C. Lee, S. Ham, Y. Hwang, S. Kwak, J. Kim, An explicit fourth-order accurate compact method for the Allen-Cahn equation, *AIMS Math.*, **9**(1) (2024), 735–762. https://doi.org/10.3934/math.2024038

28. Q. Yu, K. Wang, B. Xia, Y. Li, First and second order unconditionally energy stable schemes for topology optimization based on phase field method, *Appl. Math. Comput.*, **405** (2021), 126267. https://doi.org/10.1016/j.amc.2021.126267

29. T. Zobaer, A. Sutradhar, Maximum thickness control in topology optimization using an inflection-point-based geometric constraint, *Comput. Method. Appl. M.*, **414** (2023), 116171. https://doi.org/10.1016/j.cma.2023.116171

30. J. Liu, L. Li, Y. Ma, Uniform thickness control without pre-specifying the length scale target under the level set topology optimization framework, *Adv. Eng. Softw.*, **115** (2018), 204–216. https://doi.org/10.1016/j.advengsoft.2017.09.013

31. J. Liu, Y. Ma, A new multi-material level set topology optimization method with the length scale control capability, *Comput. Method. Appl. M.*, **329** (2018), 444–463. https://doi.org/10.1016/j.cma.2017.10.011

32. K. Crane, C. C. Weischedel, M. Wardetzky. Geodesics in heat: A new approach to computing distance based on heat flow, *ACM T. Graphic.*, **32** (2013), 152. https://doi.org/10.1145/2516971.2516977

33. T. Lee, R. L. Kashyap, C. Chu, Building skeleton models via 3-D medial surface/axis thinning algorithms, *Computer Vision, Graphics, Image Processing*, **56** (1994), 462–478. https://doi.org/10.1006/cgip.1994.1042

34. X. Yan, J. Chen, H. Hua, Y. Zhang, X. Huang, Smooth topological design of structures with minimum length scale and chamfer/round controls, *Comput. Method. Appl. M.*, **383** (2021), 113939. https://doi.org/10.1016/j.cma.2021.113939

35. M. P. Bendsøe, O. Sigmund, Topology Optimization: Theory, Methods, and Applications, Springer Science & Business Media, (2013). http://doi.org/10.1007/978-3-662-05086-6

36. O. Sigmund, K. Maute, Topology optimization approaches: A comparative review, *Struct. Multidiscip. O.*, **48** (2013), 1031–1055. https://doi.org/10.1007/s00158-013-0978-6

37. A. R. Conn, N. Gould, A. Sartenaer, Ph. L. Toint, Convergence properties of an augmented Lagrangian algorithm for optimization with a combination of general equality and linear constraints, *SIAM J. Optimiz.*, **6** (1996), 674–703. https://doi.org/10.1137/S1052623493251463

38. E. Burman, P. Hansbo, M. G. Larson, The augmented lagrangian method as a framework for stabilised methods in computational mechanics, *Arch. Comput. Methods Eng.*, **30** (2023), 2579–2604. https://doi.org/10.1007/s11831-022-09878-6

39. M. Hintermüller, M. Hinze, Moreau–Yosida regularization in state constrained elliptic control problems: Error estimates and parameter adjustment, *SIAM J. Numer. Anal.*, **47** (2009), 1666–1683. https://doi.org/10.1137/080718735

40. Y. Cai, C. Ming, Y. Qin, Skeleton extraction based on the topology and Snakes model, *Results Phys.*, **7** (2017), 373–378. https://doi.org/10.1016/j.rinp.2016.12.026

41. Y. Li, Q. Xia, S. Yoon, C. Lee, B. Lu, J. Kim, Simple and efficient volume merging method for triply periodic minimal structures, *Comput. Phys. Commun.*, **264** (2021), 107956. https://doi.org/10.1016/j.cpc.2021.107956

42. Y. Li, S. Guo, Triply periodic minimal surface using a modified Allen–Cahn equation, *Appl. Math. Comput.*, **295** (2017), 84–94. https://doi.org/10.1016/j.amc.2016.10.005

43. J. Yang, J. Kim, Unconditionally maximum principle-preserving linear method for a mass-conserved Allen–Cahn model with local Lagrange multiplier, *Commun. Nonlinear Sci.*, **139** (2024), 108327. https://doi.org/10.1016/j.cnsns.2024.108327

44. M. Wallin, N. Ivarsson, O. Amir, D. Tortorelli, Consistent boundary conditions for PDE filter regularization in topology optimization, *Struct. Multidiscip. O.*, **62** (2020), 1299–1311. https://doi.org/10.1007/s00158-020-02556-w

45. A. Clausen, E. Andreassen, On filter boundary conditions in topology optimization, *Struct. Multidisc. Optim.*, **56** (2017), 1147–1155. https://doi.org/10.1007/s00158-017-1709-1

46. S. Li, P. Zeng, N. Lin, M. Lu, J. Lin, A. Yang, Topology optimization based on improved DoubleU-Net using four boundary condition datasets, *Optim. Eng.*, **57** (2025), 884–902. https://doi.org/10.1080/0305215X.2024.2338189

47. T. Dbouk, A review about the engineering design of optimal heat transfer systems using topology optimization, *Appl. Therm. Eng.*, **112** (2017), 841–854. https://doi.org/10.1016/j.applthermaleng.2016.10.134

48. T. E. Bruns, Topology optimization of convection-dominated, steady-state heat transfer problems, *Int. J. Heat Mass Tran.*, **50** (2007), 2859–2873. https://doi.org/10.1016/j.ijheatmasstransfer.2007.01.039

49. I. Ahmed, A. E. Abouelregal, D. Atta, M. Alesemi, A fractional dual-phase-lag thermoelastic model for a solid half-space with changing thermophysical properties involving two-temperature and non-singular kernels, *AIMS Math.*, **9** (2024), 6964–6992. https://doi.org/10.3934/math.2024340

50. X. Yang, H. Li, L. Gao, Thermal-mechanical coupling topology optimization of multi-phase infill structures with a non-gradient porosity optimization method, *Int. J. Heat Mass Tran.*, **210** (2023), 124198. https://doi.org/10.1016/j.ijheatmasstransfer.2023.124198